A Graphene-like Oxygenated Carbon Nitride Material for Improved Cycle-Life Lithium/Sulfur Batteries

Jinghai Liu,*[†,§] Wanfei Li,[‡] Limei Duan,[†] Xin Li,[†] Lei Ji,[†] Zhibin Geng,[§] Keke Huang,[§] Luhua Lu,[∥] Lisha Zhou,[‡] Zongrui Liu,[†] Wei Chen,[‡] Liwei Liu,[‡] Shouhua Feng,*[§] and Yuegang Zhang*[‡]

[†]Inner Mongolia Key Lab of Chemistry of Natural Products and Synthesis of Functional Molecules, College of Chemistry and Chemical Engineering, Inner Mongolia University for the Nationalities (IMUN), Tongliao 028000, People's Republic of China

[‡]i-Lab, Suzhou Institute of Nano-Tech and Nano-Bionics, Chinese Academy of Sciences, Suzhou, 215123, People's Republic of China

[§]State Key Laboratory of Inorganic Synthesis and Preparative Chemistry, College of Chemistry, Jilin University, Changchun 130012, People's Republic of China

[∥]Faculty of Material Science and Chemistry, China University of Geosciences, Wuhan, 388 Lumo Road, Wuhan 430074, People's Republic of China

S Supporting Information

ABSTRACT: Novel sulfur (S) anchoring materials and the corresponding mechanisms for suppressing capacity fading are urgently needed to advance the performance of Li/S batteries. Here, we designed and synthesized a graphene-like oxygenated carbon nitride (OCN) host material that contains tens of micrometer scaled two-dimensional (2D) rippled sheets, micromesopores, and oxygen heteroatoms. N content can reach as high as 20.49 wt %. A sustainable approach of one-step self-supporting solid-state pyrolysis (OSSP) was developed for the low-cost and large-scale production of OCN. The urea in solid sources not only provides self-supporting atmospheres but also produces graphitic carbon nitride (g-C_3N_4) working as 2D layered templates. The S/OCN cathode can deliver a high specific capacity of 1407.6 mA h g^{-1} at C/20 rate with 84% S utilization and retain improved reversible capacity during long-term cycles at high current density. The increasing micropores, graphitic N, ether, and carboxylic O at the large sized OCN sheet favor S utilization and trapping for polysulfides.

KEYWORDS: Oxygenated carbon nitride (OCN), sulfur host, cycle life, lithium/sulfur batteries
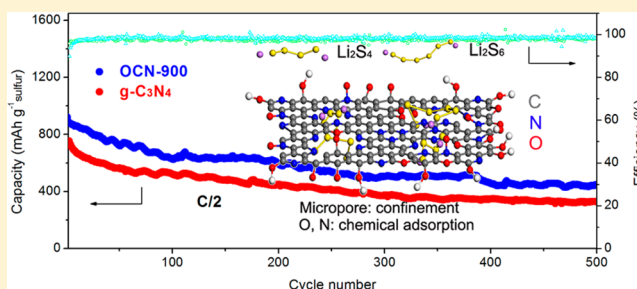
L ithium/sulfur (Li−S) batteries have recently attracted intensive research interests due to inexpensive, abundant, and nontoxic sulfur cathode with high theoretical specific capacity of 1675 mA h g^{-1} and theoretical specific energy density of ∼2600 W h kg^{-1}. Despite these considerable advantages, sulfur cathode still faces several key challenges related to capacity fading during rechargeable cycles that have prevented the practical application of Li/S batteries. The efforts in searching for better S anchoring materials have never been exhausted to suppress the dissolution of high-order polysufides, Li$_2$S$_n$ (4 ≤ n ≤ 8), in organic electrolytes[1−5] and the "shuttle effect" caused by diffusion back and forth of these soluble polysufides between the positive and negative electrodes,[6−8] which result in mass loss of active sulfur, capacity fading, and low Coulombic efficiency during cycling.

Two-dimensional (2D) materials integrating active binding sites and high surface area with porous structures for confinement of S and entrapment of the soluble polysulfides are promising host materials for S cathode to realize high specific discharge capacity with extended cycle-life. Graphene (G) with characteristics of 2D planar structure has been used to accommodate sulfur by wrapping[9−11] or supporting.[12,13] We have demonstrated that oxygenated functional groups on graphene oxides (GO) have strong chemical adsorption to anchor sulfur atoms and effectively to prevent the polysulfides from dissolving into electrolytes during cycles.[14] Nitrogen (N) in doped states or in nitrile functional groups also possesses favorable chemical interactions with discharge products, lithium polysulfides, and brings the uniform distribution and good sequestration of these discharge products in carbon hosts.[15−19] Micropores and small mesopores at G nanosheets significantly improve the accommodation capacity for sulfur and effectively confine the polysulfides into the pores instead of exterior surfaces that directly expose to the electrolytes.[20,21] Therefore, it is reasonably anticipated that a new graphene-like oxygenated carbon nitride (OCN) material bearing oxygenated functional groups, enriched nitrogen, and micromesopores in the 2D sheet would be an excellent candidate for constructing high-

performance sulfur cathode. Meanwhile, a versatile and scalable synthetic technique should be designed to prepare such material in a low-cost, environmental-friendly, and sustainable way.

Solid-state pyrolysis has been exploited to synthesize N-doped carbon nanotubes by using the organometallic complex precursors as carbon, nitrogen, and metal catalysis sources in a sealed system.[22−25] Biomass is available as abundant carbon sources. Biomass derived as small organic molecules, such as sugar[26] and glucose,[27−31] has been successfully utilized as carbon sources to obtain G. Our previous research work has shown that urea as a precursor during pyrolysis provided the self-supporting atmosphere, reactive carbon, and nitrogen sources to produce graphitic carbon nitride (g-C_3N_4), and reactive gas byproducts as pore producing agents.[32−34] Layered nitrogen-enriched g-C_3N_4 would provide the 2D reactive templates, and the biomass would work as reactive carbon and oxygen sources during pyrolysis at high temperatures. Furthermore, the escape of evolved gas from the solid products would cause the expansion forces to exfoliate the layered products. Therefore, solid-state pyrolysis with urea and biomass as reactive molecular precursors would be a sustainable approach to yield the OCN and simultaneously to produce pores without any additive assistance.

Inspired by these considerations, we designed a one-step self-supporting solid-state pyrolysis (OSSP) technique to synthesize OCN at gram scale. As schematically illustrated in Figure 1, the
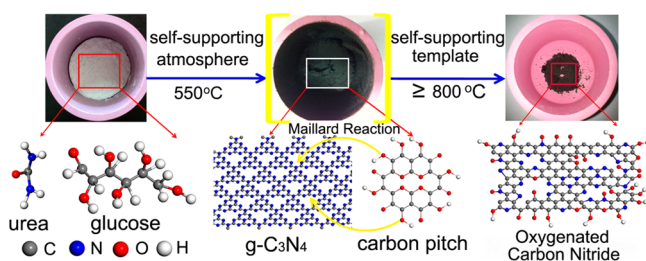

Figure 1. Schematic illustration of graphene-like OCN material prepared by OSSP.

solid carbon and nitrogen sources provided by glucose and urea were mixed together and put into a crucible. This bottom-up process conveniently accomplishes in a muffle oven at ambient pressure without protective atmosphere assistances. The temperature first arrived to 550 °C and then rose to higher temperatures (≥800 °C) by the program temperature controller (Supporting Information Figure S1). First stage of the OSSP at 550 °C, polycondensation of urea produces graphitic carbon nitride (g-C_3N_4) working as the 2D layered template and provides the self-supporting atmosphere. Simultaneously, the glucose molecules were converted into carbon pitches with oxygen-containing functional groups, which were attached on the g-C_3N_4 template (Supporting Information Figures S2−6). With pyrolytic temperature rising to higher temperatures at the second stage, the carbonyl groups on carbon pitches would react with amino groups in g-C_3N_4 template through Maillard Reaction[35,36] to chemically grafted the carbon pitches on the fringes or cavities of g-C_3N_4, where are rich in amino groups. Furthermore, the evolved gases would expand layers to finally generate the OCN sheets. The yield is in gram scale. This technology provides a low-cost and potential scale-up route for obtaining OCN material.

In order to demonstrate their graphene-like morphology, we examined morphologies and microstructures. The scanning electron microscopy (SEM) images in Figure 2a show free-standing two-dimensional (2D) sheets with typical ripples. The size is up to tens of micrometers scale. The morphology characteristics of 2D sheets were also observed at the other locations of the sample (see Figure 2a, inset). The crumpled 2D sheets was also evidently observed by transmission electron microscopy (TEM) images in Figure 2b, which are constructed by wrinkles and folded sheets at the side (see Figure 2b, inset). The results of elemental analysis reveal that the weight percent of carbon is 57.68% and nitrogen is 20.49%. Then, the weight percent for oxygen calculated to be 20.14% (see Supporting Information Table S1). As the temperature rises to 900 °C, the weight percent for carbon and nitrogen changes to 62.29 and 14.47%, respectively, while the content of oxygen remains almost constant.

The chemical structure of OCN was investigated by XPS spectra. The XPS survey spectra in Figure 2c clearly indicates the compositions consisting of carbon (C), nitrogen (N), and oxygen (O). The C 1s spectra in Figure 2d show deconvoluted five peaks with peak area ratio of 1:0.15:0.21:0.074:0.18. The carbon is mainly graphitic C with binding energy (BE) of 284.6 eV. The other four types of C are identified as sp^3 C bonded with N or O (C−N or C−O) at 285.8 eV, oxygen bridged C (C−O−C) at 286.6 eV, aromatic C bonded with N or O (C═N or C═O) at 288.1 eV and carboxyl C (C(O)OH) at 289.6 eV. For the bonding sates of nitrogen, four types of N are identified and correspond to pyridinic N at 398.2 eV, pyrrolic or pyridone N at 399.5 eV, quaternary or graphitic N at 400.1 eV, and pyridine oxide N at 402.7 eV with the peak area ratio of 1:0.63:0.67:0.48 (see Figure 2e). As to the chemical bond types of oxygen, the results in Figure 2f show four peaks with peak area ratio of 0.51:0.29:1:0.019. The main peak at 532.9 eV is identified as ether or phenol O (C−O−C or C−OH), and the other two peaks at 530.6 and 531.8 eV refer to highly conjugated forms of quinone or pyridone O, and carbonyl O (C═O), respectively. The small peak at 535.9 eV is designated as carboxylic O. Thus, a schematic illustration of the chemical structure is derived in Figure 2g.

The chemical bond types and their corresponding ratios of C, N, and O could be tuned by the OSSP. As the temperature alters from 800 to 900 °C, carbon gives five similar bonding states, but ratio of predominant graphitic C at 284.6 eV and oxygen bridged C (C−O−C) at 286.4 eV increases (see Supporting Information Figure S7b). For the four types of N, the major pyridinic N at 398.3 eV is converted into quaternary or graphitic N at 400.2 eV (see Supporting Information Figure S7c). The O is primarily in the forms of ether or phenol groups and the ratio of carboxylic O increases (see Supporting Information Figure S7d and Table S2).

The pore structures were analyzed by N_2 adsorption/desorption isotherms. As shown in Supporting Information Figure S8a, the adsorption/desorption isotherm appears a classical Type I isotherm. The strong interactions between N_2 probe molecules and pores take place at low P/P_0 ($P/P_0 < 0.1$). These features indicate that micropores are located at the OCN. The rise after $P/P_0 > 0.9$ is due to the interspaces between the layers, which would offer abundant channels for liquid electrolyte. To further demonstrate the micromesoporous structures, pore size distributions were analyzed by nonlocal density functional theory (NL-DFT) method. As shown in Supporting Information Figure S8b, a typical
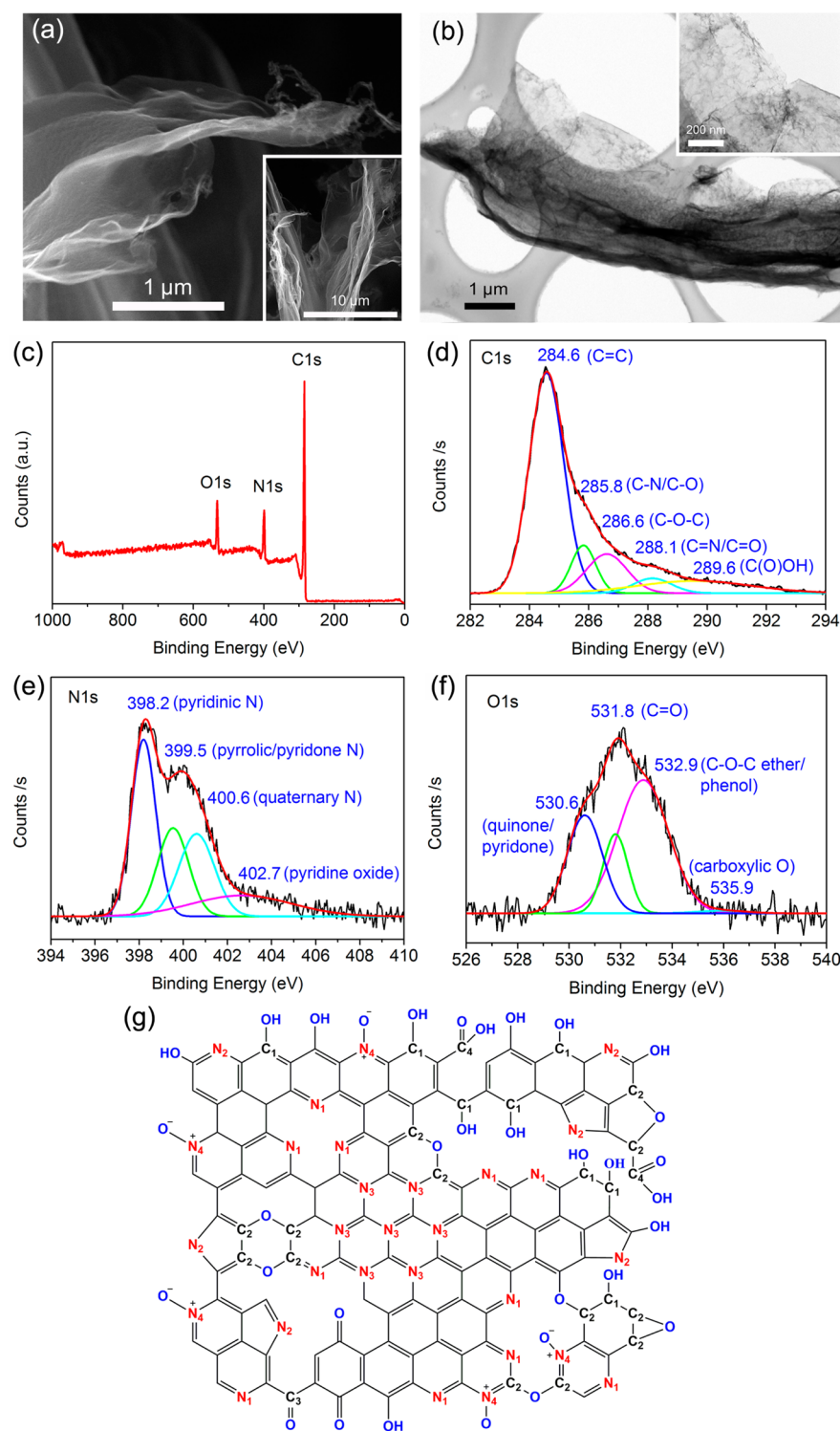
Figure 2. Morphology and chemical structure of OCN material. (a) SEM images of pristine monolith. (b) TEM images. (c) XPS survey. (d) High-resolution C 1s, (e) N 1s, and (f) O 1s XPS spectra. (g) Schematic chemical structure. N_1, pyridinic; N_2, pyrrolic/pyridone; N_3, quaternary; N_4, pyridine oxide. C_1, C−N/C-O; C_2, C−O−C; C_3, C=N/C=O; C_4, C(O)OH.

distribution of micropores (1−2 nm) is expected due to the cavities between heptazine repeating units adopted from the transient g-C_3N_4 template. Also, a well-defined narrow mesopore population centered at ca. 3.8 nm has developed. The specific surface area (SSA) is 605.97 m^2 g^{-1} derived from the Brunauer−Emmett−Teller (BET) method (Supporting Information Figure S9a).

The micromesopore volume and pore size are still affected by the OSSP. OCN from 900 °C (OCN-900) gives similar adsorption/desorption isotherms indicating the existence of micropores (Supporting Information Figure S8c). Also, typical micropores at 1.68 nm can also be observed. Interestingly, another kind of micropores centered at 1.85 nm appears (Supporting Information Figure S8d). However, the narrow

mesopores centered at ca. 3.8 nm were partly destroyed and the SSA decreases to 533.25 m^2 g^{-1}. The ratio of micropore volume determined by NL-DFT pore size distributions, however, increases from 34.07% to 57.46% (Supporting Information Table S3). Moreover, the average pore size grows from 2.8 to 3.4 nm.

The sulfur (S) was loaded on OCN sheet by a chemical deposition with a polysulfide solution followed by heat treatment. SEM images in Figure 3a reveal the agglomeration
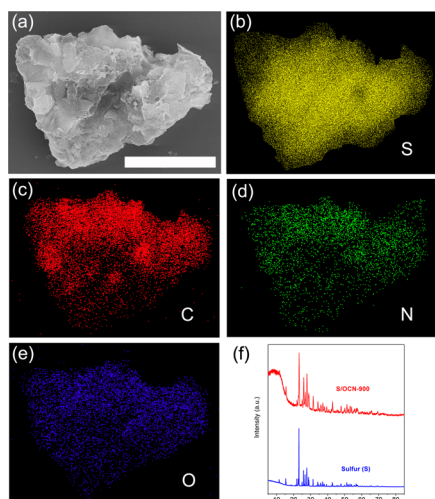

Figure 3. Sulfur/OCN nanocomposites (S/OCN-900). (a) SEM image. Scale bar 10 μm. Elemental mapping for (b) sulfur, (c) carbon, (d) nitrogen, and (e) oxygen. (f) XRD patterns of sulfur and S/OCN-900 nanocomposites.

morphology of S/OCN nanocomposites. Also, it is impossible to distinguish the S from OCN. No bulk S particles were observed, confirming the even distributions of S throughout the OCN frameworks. The elemental mappings in Figure 3b also show the uniform distributions of S. Besides, the C, N and O mappings are totally accordance with the morphology of S/OCN nanocomposite (Figure 3c−e). The scanning transmission electrons microscopy (STEM) images clearly reveal the morphology of S on the OCN sheet, where S is uniformly deposited and wrapped by the OCN 2D sheet. After S deposition and heat treatment, the planar and graphene-like morphology still retains (Supporting Information Figure S11). The successful loading of S was also demonstrated by X-ray diffraction (XRD) pattern. As shown in Figure 3f, the characteristic XRD patterns of sulfur appear for that of S/OCN nanocomposites. As indicated in the thermogravimetric analysis (TGA), about 56 wt % S was incorporated (Supporting Information Figure S12).

The electrochemical performance of S/OCN as cathode for Li−S battery was evaluated with CR2025-type coin cell. The unmodified electrolyte containing 1.0 M lithium bis-trifluoromethanesulfonylimide (LiTFSI) in a mixed solvent of 1,3-dioxolane (DOL) and 1,2-dimethoxyethane (DME) (1:1, v/v) was chosen with LiNO$_3$ (1 wt %) as an additive to passivate the lithium anode surface. Water-soluble LA132 was employed as greener binder for fabricating the cathode. Cyclic voltammetry (CV) profile in Figure 4a reveals a typical electrochemical reactions of the cathode involving in reduction and oxidation of sulfur, which was measured between 1.5 and 2.8 V (vs Li/Li$^+$) at scan rate of 0.05 mV s^{-1}. Two cathodic peaks at about 2.27

and 2.04 V and an anodic peak at 2.45 V were typical of Li/S cells. As the cycle proceeds, the cathodic peaks at 2.27 V are shifted to higher potentials and become sharper gradually along with the anodic peaks undergoing very small change, indicating an improvement of reversibility.

The S/OCN cathode (S/OCN-900) delivers an initial capacity of 1407.6 mA h g^{-1} at C/20 (with a Coulombic efficiency of about 98%), which corresponds to the S utilization of 84% (as depicted in Figure 4b). Also, the two plateaus in discharge/charge profile are related to the open ring reduction of solid S$_8$ molecules to soluble long-chain lithium polysulfides (Li$_2$S$_4$) (the higher plateau I) and the further reduction of these polysulfides to form solid Li$_2$S (the lower plateau II). Moreover, the plateau II is very flat with relatively low polarization at low rate (<C/2), which indicates the uniform deposition of insulated Li$_2$S particles on the OCN 2D sheet to suppress the charge transport resistance. The OCN host with nitrogen-rich 2D sheet and high surface area facilitates this process. While the current density switches to C/2, the discharge capacity is still 1035.7 mA h g^{-1} with a Coulombic efficiency of about 99%. From the length and slope of plateaus at 2.1 and 2.3 V,[37,38] we found that the initial capacity at C-rate lower than C/2 was controlled by the multiple steps and electrons reactions of S reduction. Next, the S/OCN cathode was subjected to cycle at various C-rates to evaluate the rate capability. As shown in Figure 4c, the reversible capacity was found to 921.8 mA h g^{-1} after the fifth cycle at C/10. Further cycling at C/5, C/2, and 1 C exhibit reversible capacity of 807.8, 651.9, and 517.3 mA h g^{-1}, respectively. When the rate switched from 1 C to C/5, the capacity was largely recovered (91.3%), indicating robustness and stability of the cathode material. Also, the sulfur utilization is further improved for OCN. The S utilization for g-C$_3$N$_4$ is only 74% with the initial discharge capacity of 1243.0 mA h g^{-1} (Figure 4d).

Long-term cycling of S/OCN at C/2 was demonstrated in Figure 4e. The S/OCN-900 delivers a reversible discharge capacity of 447.3 mA h g^{-1} over 500 cycles, indicating capacity decay of 0.1% per cycle. The cycle life can extend to 2000 cycles with useable capacity available at 230.7 mA h g^{-1}, corresponding the decay rate of 0.038% per cycle (Supporting Information Figure S14). The long-term cycling performance was also observed for S/OCN-800 and S/g-C$_3$N$_4$ cathodes. A discharge capacity of 322.7 mA h g^{-1} over 500 cycles with a capacity decay of 0.09% achieves for S/OCN-800 while 327.6 mA h g^{-1} for S/g-C$_3$N$_4$ with a decay rate of 0.11%. The ultralong cycle life over 2000 cycles can be accomplished as well (Supporting Information Figures S15 and 16). Although the decay rate is not better than these our earlier reported S hosts based on graphene oxide (GO) and N-doped G in combination with strong elastomeric binders,[39] special ionic liquid electrolytes,[14] and Li$_2$S$_x$ mediated electrolytes,[15] this is not the lowest reported value for advanced S host materials, even without optimization, where the values ranged from 0.028% to 0.48%.[38,40−42] Compared to these highest performance S hosts, the new OCN material provides a low-cost, safe processing and scale-up alternative to fabricate sulfur cathodes.

Compared to oxygen-free, low surface area, and poorly conductive g-C$_3$N$_4$ host material, the improved capacity performance is obtained for OCN-900 especially at high rates. The effects of pores, N and O chemical structures, and bulk conductivity on S utilization and capacity improvement are discussed. The OCN with average pore size in the diameter of 2.8 nm (OCN-800) and 3.4 nm (OCN-900) would
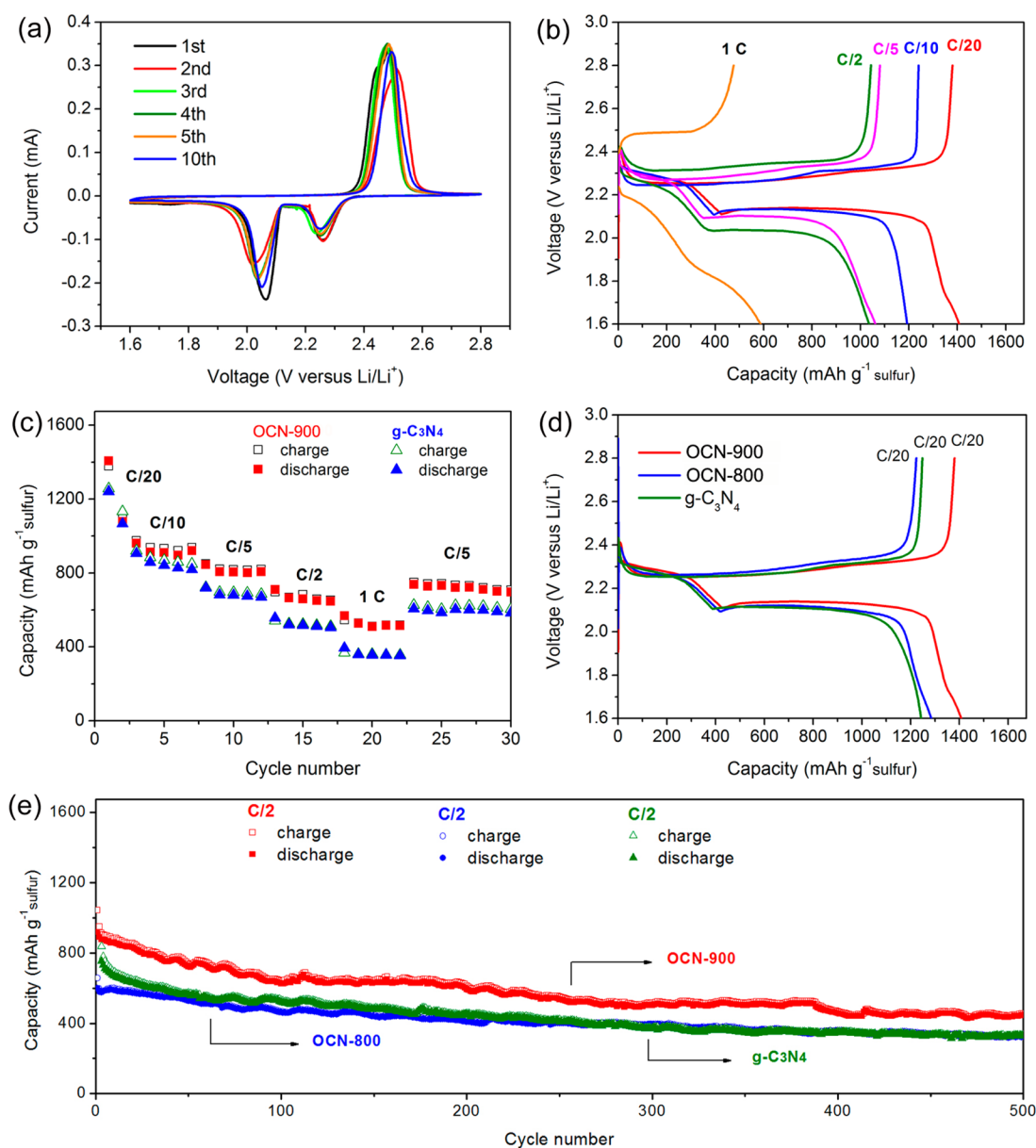
Figure 4. Electrochemical characterization of S/OCN as cathode for Li−S battery. (a) CV measured between 1.5 and 2.8 V (vs Li/Li+) for S/OCN-900 at a scanning rate of 0.05 mV s^{-1}. (b) Galvanostatic discharge−charge profiles for S/OCN-900 from C/20 to 1C (1 C = 1675 mA g^{-1}). Capacity was calculated by the mass of sulfur. (c) Rate performance of discharge−charge capacity at various rates. (d) Utilization of sulfur for OCN-800, OCN-900, and g-C$_3$N$_4$. (e) Cycling performances at C/2 after initial activation process to allow complete access of the electrolyte to the active material.

accommodate the S$_8$ molecules[4] and polysulfides[37] inside the micropores and small mesopores. The increased microporous volume ratio for OCN-900 facilitates this process. Also, the effective utilization of these confined S requires electrical contact with current collector bridged by conductive pore frameworks and access of Li+ ions through pore channels. The improved bulk conductivity (Supporting Information Table S4) and enlarged pore size for OCN-900 just demonstrate this hypothesis. The N atoms in OCN-900 are mainly graphitic N with largely decreased pyrolic N, which also contributes to the improvement of electrical conductivity and electron transfer. The ether/phenol and quinine/carbonyl typed O atoms facilitate the immobilization of S on the sheet, and the N in the carbon framework even promotes the binding energies of S with O, which has been calculated by first principle

calculations[14−17] Also, the O atoms are mainly ether/phenol O groups with increased carboxylic O for OCN-900, which promotes chemical binding interactions with polysulfides. The integration of increased micropore volume ratio, enlarged microporous channel, graphitic N, ether/phenol and carboxylic O, and strengthened electrical conductivity gives excellent performance of OCN-900.

In conclusion, an OCN host material along with an OSSP approach has been successfully developed. The S/OCN cathode presents a high S utilization efficiency and stable long-term cycle-life, which can extend to over 2000 cycles. This is attributed to the optimized OCN structures with increased micropores, graphitic N, and stable O active sites on the sheet. The strategies in this work open a promising avenue for the

advanced host of S cathode in high energy density and long cycle life Li–S batteries.

ASSOCIATED CONTENT

Ⓢ Supporting Information

Experimental details for the material preparation, characterization, and cell assembly and electrochemical measurements, along with additional supporting data. The Supporting Information is available free of charge on the ACS Publications website at DOI: 10.1021/acs.nanolett.5b01919.

AUTHOR INFORMATION

Corresponding Authors
*E-mail: ygzhang2012@sinano.ac.cn.
*E-mail: jhliu2008@sinano.ac.cn.
*E-mail: shfeng@mail.jlu.edu.cn.

Author Contributions
J. H. and W.F. contributed equally to the work.

Notes
The authors declare no competing financial interest.

ACKNOWLEDGMENTS

REFERENCES

(1) Song, M. K.; Cairns, E. J.; Zhang, Y. G. *Nanoscale* **2013**, *5*, 2186−2204.

(2) Manthiram, A.; Fu, Y. Z.; Chung, S. H.; Zu, C. X.; Su, Y. S. *Chem. Rev.* **2014**, *114*, 11751−11787.

(3) Manthiram, A.; Fu, Y. Z.; Su, Y. S. *Acc. Chem. Res.* **2013**, *46*, 1125−1134.

(4) Yin, Y. X.; Xin, S.; Guo, Y. G.; Wan, L. J. *Angew. Chem., Int. Ed.* **2013**, *52*, 2−18.

(5) Zhang, S. S. *J. Power Sources* **2013**, *231*, 153−162.

(6) Evers, S.; Nazar, L. F. *Acc. Chem. Res.* **2013**, *46*, 1135−1143.

(7) Mikhaylik, Y. V.; Akridge, J. R. *J. Electrochem. Soc.* **2004**, *151*, A1969−A1976.

(8) Yang, Y.; Zheng, G. Y.; Cui, Y. *Chem. Soc. Rev.* **2013**, *42*, 3018−3032.

(9) Lu, S. T.; Cheng, Y. W.; Wu, X. H.; Liu, J. *Nano Lett.* **2013**, *13*, 2485−2489.

(10) Evers, S.; Nazar, L. F. *Chem. Commun.* **2012**, *48*, 1233−1235.

(11) Wang, H. L.; Yang, Y.; Liang, Y. Y.; Robinson, J. T.; Li, Y. G.; Jackson, A.; Cui, Y.; Dai, H. J. *Nano Lett.* **2011**, *11*, 2644−2647.

(12) Sun, H.; Xu, G. L.; Xu, Y. F.; Sun, S. G.; Zhang, X. F.; Qiu, Y. C.; Yang, S. H. *Nano Res.* **2012**, *5*, 726−738.

(13) Zhou, W. D.; Chen, H.; Yu, Y. C.; Wang, D. L.; Cui, Z. M.; DiSalvo, F. J.; Abruna, H. D. *ACS Nano* **2013**, *7*, 8801−8808.

(14) Ji, L. W.; Rao, M. M.; Zheng, H. M.; Zhang, L.; Li, Y. C.; Duan, W. H.; Guo, J. H.; Cairns, E. J.; Zhang, Y. G. *J. Am. Chem. Soc.* **2011**, *133*, 18522−18525.

(15) Qiu, Y. C.; Li, W. F.; Zhao, W.; Li, G. Z.; Hou, Y.; Liu, M. N.; Zhou, L. S.; Ye, F. M.; Li, H. F.; Wei, Z. H.; Yang, S. H.; Duan, W. H.; Ye, Y. F.; Guo, J. H.; Zhang, Y. G. *Nano Lett.* **2014**, *14*, 4821−4827.

(16) Song, J. X.; Xu, T.; Gordin, M. L.; Zhu, P. Y.; Lv, D. P.; Jiang, Y. B.; Chen, Y. S.; Duan, Y. H.; Wang, D. H. *Adv. Funct. Mater.* **2014**, *24*, 1243−1250.

(17) Li, X.; Li, X. F.; Banis, M. N.; Wang, B. Q.; Lushington, A.; Cui, X. Y.; Li, R.; Sham, T. K.; Sun, X. L. *J. Mater. Chem. A* **2014**, *2*, 12866−12872.

(18) Guo, J. C.; Yang, Z. C.; Yu, Y. C.; Archer, L. A. *J. Am. Chem. Soc.* **2013**, *135*, 763−767.

(19) Yin, L. C.; Wang, J. L.; Lin, F. J.; Yang, J.; Nuli, Y. P. *Energy Environ. Sci.* **2012**, *5*, 6966−6972.

(20) Ding, B.; Yuan, C. Z.; Shen, L. F.; Xu, G. Y.; Nie, P.; Lai, Q. X.; Zhang, X. G. *J. Mater. Chem. A* **2013**, *1*, 1096−1101.

(21) Yang, X.; Zhang, L.; Zhang, F.; Huang, Y.; Chen, S. Y. S. *ACS Nano* **2014**, *8*, 5208−5215.

(22) Zhi, L. J.; Gorelik, T.; Friedlein, R.; Wu, J.; Kolb, U.; Salaneck, W. R.; Mullen, K. *Small* **2005**, *1*, 798−801.

(23) Hamaoui, B. E.; Zhi, L. J.; Wu, J. S.; Kolb, U.; Mullen, K. *Adv. Mater.* **2005**, *17*, 2957−2960.

(24) Su, P. P.; Xiao, H.; Zhao, J.; Yao, Y.; Shao, Z. G.; Li, C.; Yang, Q. H. *Chem. Sci.* **2013**, *4*, 2941−2946.

(25) Wang, L.; Tian, C. G.; Wang, B. L.; Wang, R. H.; Zhou, W.; Fu, H. G. *Chem. Commun.* **2008**, 5411−5413.

(26) Pan, F. P.; Jin, J. T.; Fu, X. G.; Liu, Q.; Zhang, J. Y. *ACS Appl. Mater. Interfaces* **2013**, *5*, 11108−11114.

(27) Zhang, Y. W.; Ge, J.; Wang, L.; Wang, D. H.; Ding, F.; Tao, X. M.; Chen, W. *Sci. Rep.* **2013**, *3* (2771), 1−8.

(28) Li, X. H.; Kurasch, S.; Kaiser, U.; Antonietti, M. *Angew. Chem., Int. Ed.* **2012**, *51*, 9689−9692.

(29) Tian, L. L.; Wei, X. Y.; Zhuang, Q. C.; Jiang, C. H.; Wu, C.; Ma, G. Y.; Zhao, X.; Zong, Z. M.; Sun, S. G. *Nanoscale* **2014**, *6*, 6075−6083.

(30) Li, X. H.; Antonietti, M. *Angew. Chem., Int. Ed.* **2013**, *52*, 4572−4576.

(31) Wang, X. B.; Zhang, Y. J.; Zhi, C. Y.; Wang, X.; Tang, D. M.; Xu, Y. B.; Weng, Q. H.; Jiang, X. F.; Mitome, M.; Golberg, D.; Bando, Y. *Nat. Commun.* **2013**, *4* (2905), 1−8.

(32) Liu, J. H.; Zhang, T.; Wang, Z. C.; Dawson, G.; Chen, W. *J. Mater. Chem.* **2011**, *21*, 14398−14401.

(33) Liu, J. H.; Zhang, Y. W.; Lu, L. H.; Wu, G.; Chen, W. *Chem. Commun.* **2012**, *48*, 8826−8828.

(34) Zhang, Y. W.; Liu, J. H.; Sui, Y.; Chen, W. *Nanoscale* **2012**, *4*, 5300−5303.

(35) Hodge, J. E. *J. Agric. Food Chem.* **1953**, *1*, 928−943.

(36) Zheng, J. M.; Gu, M.; Wagner, M. J.; Hays, K. A.; Li, X. H.; Zuo, P. J.; Wang, C. M.; Zhang, J. G.; Liu, J.; Xiao, J. *J. Electrochem. Soc.* **2013**, *160*, A1624−A1628.

(37) Su, Y. S.; Manthiram, A. *Nat. Commun.* **2012**, *3* (1166), 1−8.

(38) Su, Y. S.; Fu, Y. Z.; Cochell, T.; Manthiram, A. *Nat. Commun.* **2013**, *4* (2985), 1−8.

(39) Song, M. K.; Zhang, Y. G.; Cairns, E. J. *Nano Lett.* **2013**, *13*, 5891−5899.

(40) Liang, X.; Garsuch, A.; Nazar, L. F. *Angew. Chem., Int. Ed.* **2015**, *54*, 3907−3911.

(41) Liang, X.; Hart, C.; Pang, Q.; Garsuch, A.; Weiss, T.; Nazar, L. F. *Nat. Commun.* **2015**, *6* (5682), 1−8.

(42) Seh, Z. W.; Li, W. Y.; Cha, J. J.; Zheng, G. Y.; Yang, Y.; McDowell, M. T.; Hsu, P. C.; Cui, Y. *Nat. Commun.* **2013**, *4* (1331), 1−8.